Estimation of sea ice thickness distributions through the combination of snow depth and satellite laser altimetry data

24th July 2009

Nathan T. Kurtz[1], Thorsten Markus[2], Donald J. Cavalieri[2], Lynn C. Sparling[1], William B. Krabill[3], Albin J. Gasiewski[4], John G. Sonntag[5]

[1]Department of Physics, University of Maryland, Baltimore County, Baltimore, MD 21250

[2]Hydrospheric and Biospheric Sciences Laboratory, NASA Goddard Space Flight Center, Greenbelt, MD 20771

[3]NASA Goddard Space Flight Center/Wallops Flight Facility, Wallops Island, VA 23337

[4]Department of Electrical and Computer Engineering, University of Colorado, Boulder, CO 80309

[5]EG&G Technical Services/NASA Goddard Space Flight Center/Wallops Flight Facility, Wallops Island, VA 23337

Abstract

Combinations of sea ice freeboard and snow depth measurements from satellite data have the potential to provide a means to derive global sea ice thickness values. However, large differences in spatial coverage and resolution between the measurements lead to uncertainties when combining the data. High resolution airborne laser altimeter retrievals of snow-ice freeboard and passive microwave retrievals of snow depth taken in March 2006 provide insight into the spatial variability of these quantities as well as optimal methods for combining high resolution satellite altimeter measurements with low resolution snow depth data. The aircraft measurements show a relationship between freeboard and snow depth for thin ice allowing the development of a method for estimating sea ice thickness from satellite laser altimetry data at their full spatial resolution. This method is used to estimate snow and ice thicknesses for the Arctic basin through the combination of freeboard data from ICESat, snow depth data over first-year ice from AMSR-E, and snow depth over multiyear ice from climatological data. Due to the non-linear dependence of heat flux on ice thickness, the impact on heat flux calculations when maintaining the full resolution of the ICESat data for ice thickness estimates is explored for typical winter conditions. Calculations of the basin-wide mean heat flux and ice growth rate using snow and ice thickness values at the ~70 m spatial resolution of ICESat are found to be approximately one-third higher than those calculated from 25 km mean ice thickness values.

1 Introduction

Sea ice is an important component and indicator of change in the global climate system. While the extent of the Arctic and Antarctic sea ice covers has been measured for some time, sea ice thickness values are needed to obtain the mass balance which will offer a much more complete assessment of the state of the global sea ice cover. For this reason, the determination of sea ice thickness is part of the mission objectives for NASA's current Ice, Cloud, and Land Elevation Satellite (ICESat) mission (*Zwally et al.*, 2002) as well as ESA's upcoming Cryosat-2 mission. Recent efforts have led to the development of methods for the retrieval of the sea ice freeboard from satellite altimetry data (e.g. *Farrell et al.*, 2009; *Forsberg and Skourup*, 2005; *Kwok et al.*, 2007; *Peacock and Laxon*, 2004). By combining these freeboard values with snow depth data sets, estimations of mean sea ice thickness values from satellite data on spatial scales of 25 km and larger have been made (e.g. *Kwok and Cunningham*, 2008; *Laxon et al.*, 2003; *Spreen et al.*, 2006; *Zwally et al.*, 2008). However, an unknown factor in these studies has been how to combine the freeboard and snow depth values given the generally large differences in spatial resolution of the data sets. Currently, little is known about the distribution of snow at the length scales of the altimetry data. A better understanding of the distribution of snow at the altimeter length scales should be useful to efforts to derive sea ice thickness values from the combination of snow depth and altimetry data.

Altimeters do not directly measure sea ice thickness, rather, they measure surface elevation. When combined with sea surface elevation measurements, surface elevation can be converted to the height above sea level of the ice (freeboard or fb), or snow (h_s) and ice together (snow-ice freeboard or $h_s + fb$) depending on the type of altimeter used. The sea

ice thickness (h_i) can then be found by solving the equation for hydrostatic balance

$$h_i = \frac{\rho_s}{\rho_w - \rho_i} h_s + \frac{\rho_w}{\rho_w - \rho_i} fb \tag{1}$$

where ρ_s, ρ_i, and ρ_w are the densities of the snow, the sea ice, and the water, respectively. Laser altimeters such as ICESat retrieve $h_s + fb$ while satellite radar altimeters such as Cryosat-2 and Envisat retrieve fb, thus knowledge of snow depth is required to convert altimetry measurements to sea ice thickness. Snow depth can be obtained from satellite passive microwave data (for example, Advanced Microwave Scanning Radiometer - EOS [AMSR-E]), can be estimated from model precipitation analyses (for example, National Centers for Environmental Prediction-National Center for Atmospheric Research reanalysis data, European Centre for Medium-Range Weather Forecasts [ECMWF] data), estimated from climatological values compiled by *Warren et al.*, [1999], or can be derived from a combination of coincident laser and radar altimetry data because of the difference in penetration of snow between these measurements. Satellite measurements of freeboard and snow depth are made at very different resolutions, thus combining the data to derive sea ice thickness is not a straightforward process. The specific objective of this paper is to use high resolution aircraft data to analyze the spatial variability of the snow-ice freeboard and snow depth at scales ranging from 50 m (scale of ICESat data), to 12 km (scale of AMSR-E snow depth), to 25 km and larger (scale of model precipitation analysis e.g. 1.125° for ECMWF data). The goal is to provide a basis for an optimal combination of the generally low resolution snow depth measurements with high resolution laser altimetry products from ICESat to obtain the sea ice thickness.

It is more convenient to recast equation (1) in terms of the snow-ice freeboard since this

is what is retrieved by the laser altimeter used in this study. Denoting the snow-ice freeboard by $fb_{si} = h_s + fb$, equation (1) becomes

$$h_i = \frac{\rho_w}{\rho_w - \rho_i} fb_{si} - \frac{\rho_w - \rho_s}{\rho_w - \rho_i} h_s \tag{2}$$

The estimation of h_i from satellite measurements of h_s and fb_{si} is thus problematic because they have different resolutions and coverages. Another difficulty is that the ice and snow densities are not completely known, and may depend on the ice thickness (*Kovacs et al.*, 1996), snow depth and snow age (*Sturm and Benson,* 1997). In the following we assume that ρ_i and ρ_s are constant for lack of specific density information. This assumption will lead to errors in the estimated ice thickness and ice thickness dependent parameters presented here. However, *Kwok and Cunningham*, [2008] estimate uncertainties in the snow and ice density values account for only ~10-20% of the variance in ice thickness estimates for the Arctic. Most of the variance is due to uncertainties in the freeboard and snow depth values. It is also important to note that the impact of the uncertainty in ρ_s is lessened when formulating the problem in terms of h_s and fb_{si} (Eq. 2) instead of in terms of h_s and fb (Eq.1). The reason is that some of the uncertainty in ρ_s is removed when the combined snow-ice freeboard fb_{si} is measured because ρ_s appears only in a density difference term.

There are two approaches to combining the snow depth and snow-ice freeboard measurements. The first is a method in which the high resolution freeboard measurements are scaled up to the larger scale snow depth measurement by averaging. The result is a sea ice thickness estimate on the scale of the snow depth measurement or larger. Spatially averaging equation (2) gives

$$H_i = \frac{\rho_w}{\rho_w - \rho_i} F - \frac{\rho_w - \rho_s}{\rho_w - \rho_i} H_s \tag{3}$$

where we use capital letters H_i, H_s, and F to denote the sea ice thickness, snow depth, and snow-ice freeboard, respectively, averaged over a scale equal to or greater than the snow depth measurement (12 km or greater). If the averaging is over the snow depth measurement scale, then H_s represents a single snow depth measurement while F is generally an average over many altimeter measurements.

The second approach retains the actual altimeter resolution and scales the snow depth measurement to the resolution of the altimeter resulting in a sea ice thickness estimate on the scale of the much higher resolution altimeter measurement. We show that this scaling can be accomplished using relationships between the mean snow depth of an area (determined from e.g. AMSR-E) and the local snow-ice freeboard measurements of the altimeter (determined from ICESat). Calculation of the sea ice thickness at the scale of the altimeter allows the derivation of the sea ice thickness distribution function, $g(h)$, within the area of the snow depth measurement. Following *Thorndike et al.* [1975], we define $g(h)$ as follows: Consider a region $\mathbf{R}$ in the ice pack encompassing a snow depth measurement with area R. Let $A(h_1, h_2)$ be the area within $\mathbf{R}$ covered by ice of thickness h in the range $h_1 \leq h < h_2$; the ice thickness distribution $g(h)$ is then defined as

$$\int_{h_1}^{h_2} g(h)dh = \frac{1}{R} A(h_1, h_2) \tag{4}$$

Knowledge of $g(h)$ has advantages over H_i for sea ice dynamics because the amount of thin ice is needed to gauge the strength of the ice pack in resistance to compression,

while the amount of ridging affects the wind and water drag on the ice (*Thorndike et al.,* 1975). Thermodynamically, knowledge of $g(h)$ is more important than H_i because of the large heat flux and increased absorption of shortwave radiation that occurs mainly over ice with a thickness less than 1 m (*Maykut,* 1978). For example, if 60% of a region in the Arctic contains ice with a thickness of 1.5 m and the other 40% of the region contains ice with a thickness of 0.2 m a typical ocean to atmosphere heat flux for the region would be 80 $W\,m^{-2}$. However, the heat flux calculated using the large-scale average ice thickness of the region ($H_i = 1.0\,m$) is only half as much with a value of 40 $W\,m^{-2}$. Better knowledge of $g(h)$ has also been found to be necessary for modeling the oceanic and atmospheric circulations (*Holland et al.,* 2006) and to better understand the ice-albedo feedback mechanism (*Curry et al.,* 1995).

An uncertainty with both ice thickness retrieval methods is that the true spatial average over the snow depth grid cell may not be well represented by the average across the available altimeter track if the local variability is strong. After the description of the data (Section 2) we begin the analysis in Section 3 by studying the impact of the spatial variability of snow depth on the derived ice thickness values. We then estimate the uncertainties that are introduced when combining high resolution altimeter measurements with low resolution snow depth measurements. Section 4 presents a method to combine satellite retrieved snow depth and snow-ice freeboard data to derive the sea ice thickness distribution function, $g(h)$. The thermodynamic implications of the derived value of $g(h)$ for the Arctic are explored in Section 5.

2 Data

In March 2006 a field campaign to validate the EOS Aqua AMSR-E sea ice snow depth product was successfully completed (*Cavalieri and Markus*, 2006). An array of instruments mounted on the NASA P-3 aircraft were used to measure properties of the snow and sea ice, in particular the snow depth and elevation. Measurements were taken in several different areas of the Arctic (Figure 1) which were chosen to represent distinct sea ice covers with different snow depths seen in AMSR-E data (*Cavalieri and Markus*, 2006). The March 21 and 22 flights were over first year ice types while the March 24 and 25 flights were over a mixture of first year and multiyear ice (as observed in RADARSAT data). The flights on March 21, 22, and 25 each cover an area of approximately 50 km x 100 km with parallel lines separated by approximately 5 km. The intent was to cover those areas as densely as possible.

Two key instruments that were flown on the P-3 and used for this study are the Airborne Topographic Mapper (ATM) (*Krabill et al.*, 1995) and the Polarimetric Scanning Radiometer (PSR) (*Piepmeier and Gasiewski*, 1996). The ATM is a conically-scanning laser altimeter that provides elevation measurements referenced to the ITRF-2000 reference frame and projected onto the WGS-84 ellipsoid for each laser pulse reflected from the surface. The reflection of the laser pulse occurs at the top of the snow surface in the case of snow-covered ice allowing the determination of the snow-ice elevation. Comparisons with other ATM flights and in-situ results indicate that the accuracy of the ATM is about 10 cm or better (*Krabill et al.*, 1995) with an estimated precision of $\sim$2 cm. The aircraft altitude was around 200 m for all data sets which gives a swath width of $\sim$100 m and footprint size of 0.5 m for the ATM data.

To convert the ATM elevation data into snow-ice freeboard, the local sea level must be

known for each point and subtracted from the elevation data. Sea level is not a constant over the spatial and temporal scales of the aircraft measurements; it is a function of many factors including the geoid, dynamic topography, tides, and atmospheric pressure, with the geoid and tides being the most dominant factors for our study areas. Tidal effects have been removed from the ATM data using solutions from the TPX07.1 tidal model (*Egbert and Erofeeva, 2002*). To remove effects due to the geoid, the ArcGP geoid (*Kenyon and Forsberg*, 2001), which has a grid spacing of 5' x 10' (latitude x longitude), was bilinearly interpolated and subtracted from the elevation data. The mean elevation of all points within 25 km of each measurement was then removed to function as a type of high pass filter to further reduce large scale residuals in the geoid (following *Kwok et al.*, 2007). Once these time and spatially varying components of the sea level are removed, the sea level for a larger area can be estimated by periodically using the elevation of open water as a reference sea level. These open water points were found by analyzing coincident aerial photography to find leads, or breaks in the sea ice cover. To reduce noise, the 0.5 m footprint sized ATM data was averaged over a circle 7 m in diameter over each region identified in a photograph containing open water. The minimum of the 7 m averaged elevation measurements within each photographed region was then selected as sea level. Since there were many sea level measurements made within the entire study area, the reference sea surface height for each elevation measurement, h_{SL}, was calculated by the distance weighted average of the nearby sea level estimates

$$h_{SL} = \sum_i w_i h_{SL}^i \tag{5}$$

where w_i is the normalized weight calculated as

$$w_i = \frac{\sum_j^N d_j}{d_i} \tag{6}$$

The numerator is the sum of all distances between the measured elevation point and the sea level measurement point within 40 km, the denominator, d_i, is the distance between the measured point and each sea level point i within 40 km. The weights were chosen in this manner to give a higher weight to closer measurements since the quality of the sea level estimate decreases with increasing distance between the elevation and sea level measurements. The snow-ice freeboard was then calculated by subtracting the local sea level estimate from the elevation measurement. It was then gridded to a 50 m polar stereographic projection grid for ease of computation and the similarity to the ICESat footprint size of approximately 50 m for this time period.

Snow depths were derived using the Polarimetric Scanning Radiometer (PSR) on board the P-3. The PSR is a passive microwave radiometer with similar channels to the AMSR-E or Special Sensor Microwave Imager (SSM/I) radiometers. Snow depth is derived from the PSR data using the algorithm of *Markus and Cavalieri* [1998]. The footprint size is approximately 64 m for the altitude flown during the campaign. PSR-derived snow depth was gridded to the same 50 m polar stereographic projection as the snow-ice freeboard data. Snow depth was not derived for the March 24 and 25 data sets as these regions contain multiyear ice which can lead to large errors in the retrieved snow depth value because of the radiometric ambiguity between multiyear ice and deep snow (*Comiso et al.*, 2003).

The satellite analogues of the ATM and PSR instruments (ICESat and AMSR-E, respec-

tively) are used to retrieve freeboard and snow depth values for the seasonal ice zones in the Arctic. Snow depth values of first-year ice areas are derived from AMSR-E daily brightness temperature data using the algorithm of *Markus and Cavalieri* [1998]. Over the perennial ice zone, freeboard is retrieved from ICESat data while snow depth is taken from the climatology of *Warren et al.*, [1999]. A sea ice freeboard product does not currently exist for the ICESat satellite so additional processing must be done in order to convert the elevation data product into a snow-ice freeboard. *Kurtz et al.* [2008] showed that elevation data from ICESat compares quite well with ATM observations under favorable atmospheric conditions. They found RMS differences of 16-21 cm between the ATM and ICESat elevation measurements and a bias of less than 2 cm. The conversion of ICESat elevation data into snow-ice freeboard has been shown to be possible in several studies (e.g. *Kwok et al.*, 2007; *Kurtz et al.*, 2008; *Farrell et al.*, 2009) as long as an adequate algorithm for finding sea surface reference points is used.

In a similar manner to the method used to calculate snow-ice freeboard from the ATM data, snow-ice freeboard is calculated from ICESat elevation data, h_e, by subtracting out the local sea level elevation

$$fb_{si} = h_e - h_{SL} \tag{7}$$

Kwok et al. [2007] detail three methods to identify sea surface tiepoints in ICESat data, the elevations of the tiepoints are then used to find the local sea level elevation within a 25 km transect. In this study, we use the method which identifies sea surface tiepoints from data which have an elevation below an expected deviation from the local mean surface (designated

as H_σ in *Kwok et al.* [2007]). The reader is referred to *Kwok et al.* [2007] for a more detailed description of this and other methods used to find sea surface tiepoints.

3 Impact of sub-grid cell snow depth variability on ice thickness retrievals

Satellite altimetry provides only a relatively narrow line of data through the comparatively large grid cell of satellite passive microwave or model derived snow depth data. Because freeboard values from satellite altimeters and snow depth values from satellite or model data are provided at different spatial resolutions, we wish to quantify the error in assuming the large-scale snow depth value is representative of the snow depth actually encountered along an ICESat track. We do this by using the high resolution aircraft snow depth data to simulate snow depth measurements made at the resolution of satellite passive microwave and model snow depth grid cells. We then compare the simulated low resolution snow depth to that encountered along a single flight track segment within the grid cell. Figure 2 shows an example aircraft flight path and the development of the approach. Let

$$\delta^i = S^i - < S > \tag{8}$$

where S^i is the mean snow depth of one segment of the aircraft track within a snow depth grid cell, $< S >$ is the mean of all segments S^i which lie within a specific snow depth grid cell. Proceeding in this manner for $i = 1 : N$, where N is the number of segments within the study area, we build up a set of values $\delta^{1:N}$, representing the difference between the mean

snow depth of a grid cell and the average snow depth encountered along a single flight track segment within the cell. Since the distribution of $\delta^{1:N}$ is approximately Gaussian in shape for all grid cell sizes studied (Figure 3), we take the standard deviation of $\delta^{1:N}$ as our estimate of the uncertainty in using the snow depth derived from satellite passive microwave or model data as the mean snow depth along an ICESat track. This uncertainty is due mainly to the spatial variability of snow depth within the grid cell.

Results of the snow depth uncertainty estimates can be seen in Table 1 for grid cell sizes ranging from an AMSR-E passive microwave snow depth grid cell (12 km) to a model grid cell (25 km and 50 km). The observed uncertainties appear to be relatively insensitive to the size of the snow depth grid cell used. Since the primary reason for combining the altimeter and snow depth data sets is to find the sea ice thickness, it is necessary to consider the effect of this snow depth uncertainty on the sea ice thickness retrieval error. Rewriting equation (3) in terms of the laser altimetry measured parameter of snow-ice freeboard scaled to the resolution of the snow depth, F, and using constant bulk densities of 320 $\frac{kg}{m^3}$ for snow, 1024 $\frac{kg}{m^3}$ for water, and 915 $\frac{kg}{m^3}$ for the sea ice gives

$$H_i = 9.39F - 6.46H_s \tag{9}$$

where H_i is the average sea ice thickness at the resolution of the snow depth grid cell. The uncertainty in snow depth due to spatial variability of snow across a large-scale satellite or model snow depth grid cell will then introduce an uncertainty, or error, in the H_s term which is multiplied by a factor of 6.46 when converted to ice thickness. Using the snow depth uncertainty from Table 1 for an AMSR-E sized snow depth grid cell gives an error

in ice thickness due to spatial variability of snow within a grid cell of 16 cm and 23 cm for the March 21 and March 22 data sets, respectively. For comparison, retrieval errors of F and H_s from satellite data are estimated to be 5 cm for both ICESat freeboard (*Kwok and Cunningham*, 2008) and AMSR-E snow depth retrievals (*Comiso et al.*, 2003) leading to ice thickness retrieval errors of 47 cm and 32 cm from the retrieval errors of the freeboard and snow depth, respectively.

Spreen et al [2006] include the effect of the uncertainties of snow and ice densities and give the following expression for the uncertainty of the ice thickness value calculated using equation (3)

$$\sigma_{H_i} = \left[\left(\frac{\rho_w}{\rho_w - \rho_i} \right)^2 \sigma_F^2 + \left(\frac{\rho_s - \rho_w}{\rho_w - \rho_i} \right)^2 \sigma_{H_s}^2 + \left(\frac{H_s \left(\rho_s - \rho_w \right) + F \rho_w}{\left(\rho_w - \rho_i \right)^2} \right)^2 \sigma_{\rho_i}^2 + \left(\frac{H_s}{\rho_w - \rho_i} \right)^2 \sigma_{\rho_s}^2 \right]^{\frac{1}{2}} \tag{10}$$

where σ_F, σ_{H_s}, σ_{ρ_s}, and σ_{ρ_i} are the uncertainties of the freeboard, snow depth, and densities of snow and ice, respectively. The snow depth uncertainty term, σ_{H_s}, is a combination of the retrieval uncertainty from the satellite or model data and the uncertainty due to spatial variability of snow depth within the grid cell. It is not possible to find the sub-grid cell variability of snow depth for the whole of the Arctic. Nonetheless, it is useful to have an estimate of this quantity for climatological comparisons of ice thickness data. The uncertainties shown in Table 1 are independent of grid cell size but show differences between the March 21 and 22 data sets, which may be due to the different ice regimes of the survey locations. However, as a percentage of the mean snow depth for the March 21 and 22 areas (shown in Table 2), the uncertainties are similar at about 13% of the mean. With only two data sets (March 21 and

March 22) it is not possible to say whether the variability of snow within a large-scale grid cell is a linear function of the mean, but it can serve as an error estimate when combining or comparing satellite altimetry and snow depth data sets (e.g. *Maksym and Markus*, 2008). Using this estimate, the $\sigma^2_{H_s}$ term in equation (10) can then be rewritten as

$$\sigma^2_{H_s} \approx \sigma^2_{H_{retrieval}} + (.13H_s)^2 \tag{11}$$

where $\sigma_{H_{retrieval}}$ is the retrieval uncertainty of the snow depth from the satellite or model data.

4 Scaling of large-scale snow depth data to the altimeter resolution

We now present a method to scale the snow depth measurement to the size of the freeboard measurement in order to derive a high resolution sea ice thickness distribution. The previous analysis has shown that snow depth has low spatial variability on scales comparable to satellite passive microwave measurements or model results. This low spatial variability allows us to use the passive microwave or model snow depth as an approximation for the mean snow depth along the altimeter track. If hs_{AMSR-E} is the snow depth value measured over a 12.5 km x 12.5 km area by AMSR-E and if we have N altimeter measurements within that area then

$$hs_{AMSR-E} \approx \sum_{i=1}^{N} \frac{hs_i}{N} \tag{12}$$

where hs_i is the snow depth at each altimeter measurement. Rather than use the same

snow depth (hs_{AMSR-E}) for all altimeter measurements, our goal is to find $hs_{1:N}$ using this relation as a constraint.

4.1 Altimeter-scale snow depth distribution

Based on analyses of in-situ data from the Arctic and Antarctic (e.g. *Sturm et al.*, 2006, *Tin and Jeffries*, 2001, *Massom et al.*, 1997), we expect to be able to infer a sub-grid cell snow depth distribution by utilizing relationships between snow depth and sea ice thickness, freeboard, roughness, and surface reflectivity. For example, we expect points with low reflectivity at wavelengths used by laser altimeters to have little to no snow cover so that we can infer sea ice thickness directly from the freeboard estimate. We also expect that, on average, the large-scale nature of precipitation events will evenly distribute the snow depth across ice of the same age. Younger and thinner ice will not have experienced as many precipitation events and may have a smaller snow depth and therefore a lower measured snow-ice freeboard. However, wind-blown redistribution of snow complicates this picture as snow can be blown from thicker to thinner ice areas and can preferentially collect in rougher areas. The complex nature of factors involved in the distribution of snow at the small length scales used by altimeters motivates an empirical approach based on observations.

We explore the relationship between snow depth and the snow-ice freeboard for the 50 m grid points of our study area over a length scale of 12.5 km. This provides the highest spatial scale with which we can combine AMSR-E snow depths with ICESat altimetry measurements to derive the sea ice thickness. An analysis of the gridded aircraft laser altimetry and PSR snow depth data revealed a common feature within each 12.5 km transect which is most likely due to the mixture of sea ice types with different ages and snow histories. The snow

depth increased with increasing snow-ice freeboard approximately linearly until it reached a saturation point where the snow depth appeared to be randomly distributed around a common mean (Figure 4). The sea ice below the saturation point is most likely young and recently formed sea ice with a relatively new snow cover, while sea ice above the saturation point is most likely older sea ice with a much longer history of snow accumulation.

To resolve the snow depth for each altimeter point we need to know the maximum snow-ice freeboard where the snow depth stops increasing linearly with increasing freeboard (fb_{cutoff}), and the mean value of the snow depth for points with a snow-ice freeboard higher than fb_{cutoff}. We found fb_{cutoff} to be related to the mean snow depth and snow-ice freeboard of the region. This motivates the use of a multiple regression formulation to derive a mathematical relationship between fb_{cutoff} and these values from observations. Our observations consisted of a sample of 91 12.5 km segments where fb_{cutoff} values were selected based on visual inspection of plots similar to those shown in Figure 4. The result of the multiple linear regression to predict fb_{cutoff} is

$$fb_{cutoff} = 0.69H_s + .22F + 5.10 \tag{13}$$

where F and H_s are the mean values in cm of snow-ice freeboard and snow depth for the 12.5 km transect, respectively. The regression has a correlation of 0.75. The mean and standard deviation of the difference of the predicted fb_{cutoff} with the visually derived values is 0.2 cm and 4.4 cm, respectively. The results of the regression in comparison to the cutoff values with the visually derived values are shown in Figure 5, while some scatter is evident in the plot the overall relationship appears valid.

For points with snow-ice freeboards above the cutoff value we need to find the snow depth, hs_{thick}, to assign to all points above the freeboard cutoff. A regression of the values of hs_{thick} calculated from the visually derived data sets gives the relationship between hs_{thick} and the mean snow depth of the region to be

$$hs_{thick} = aH_s + 0.83 \tag{14}$$

where H_s is the mean snow depth in cm for the entire 12.5 km region, and $a = 1.03$. a was found to vary between 0.97 and 1.13. Points above the cutoff value have a snow depth slightly above the mean value for the region to compensate for the lower snow depth used for freeboards less than fb_{cutoff}. As can be seen in Figure 4, the variability of snow depth for points above the cutoff value can be quite high (note that this snow depth variability is at a much different scale than that found in Section 3). The observed standard deviations of snow depth are about one-third of the mean. A similar variability of snow depth over multiyear ice from 1 km lines of in-situ data was also observed by *Warren et al.*, [1999]. Despite this large snow depth variability, assigning a mean snow depth to all points above the freeboard cut-off should still produce useful sea ice thickness results because 1) for large freeboard values the weight of the snow becomes less important; 2) the average snow depth is conserved in this method (discussed below) so that the average of all ice thickness values is the same as when using just the 12.5 km (or larger) average; 3) for heat flux calculations (discussed in the next section) errors in snow and ice thickness values of these thicker ice points are of small importance.

Finally, to determine the relationship between snow depth and the snow-ice freeboard for

points below the freeboard cutoff we use a simple linear fit of the freeboard as a function of the cutoff value. The resulting snow depth for each individual altimetry point with snow-ice freeboard less than fb_{cutoff}, hs_{thin} is

$$hs^i_{thin} = hs_{thick}\left(\frac{fb^i_{si}}{fb_{cutoff}}\right) \tag{15}$$

where hs^i_{thin} is the snow depth for each point i that is below the freeboard cutoff and fb^i_{si} is the snow-ice freeboard of measurement i. We might expect that points with values of fb_{si} of only several centimeters are thin ice which has not had time to accumulate a snow cover, indeed Figure 4(b) shows this can be the case. The data sets used in this study did not provide a way to sufficiently predict where the transition from snow-free to snow-covered ice occurs, but surface reflectivity data available to laser altimeters could potentially be used to distinguish between these regions. The standard deviation of the difference between the predicted values of hs_{thin} and the observed snow depths is 5.3 cm.

This method does not necessarily constrain the assigned snow depths to the mean value (equation 12). In order to properly constrain the assigned snow depths an iterative method was used to adjust hs_{thick} with an associated adjustment to hs_{thin} until a difference between H_s and $\sum \frac{hs_i}{N}$ of less than .5 cm was found. Convergence typically happened within 1 iteration due to the nature of the adjustment.

The steps for assigning different snow depth values for each altimeter footprint can be summarized as follows:

1) Find the mean snow depth of a region (e.g. from passive microwave or model data) and the mean snow-ice freeboard from the corresponding altimetry data and use equation

(13) to find fb_{cutoff}.

2) Calculate the snow depth value hs_{thick} using equation (14).

3) Use hs_{thick} to assign snow depth for points where the snow-ice freeboard is greater than fb_{cutoff} and use equation (15) to assign snow depth for points with snow-ice freeboard less than fb_{cutoff}.

4) Calculate the mean snow depth assigned to all altimeter points in step 3 and find the difference with the passive microwave or model snow depth.

5) Adjust hs_{thick} by the difference computed in step 4. Repeat steps 3-5 until the difference computed in step 4 is small ($<$ .5 cm).

4.2 Comparison of results with observed ice thickness distributions

Figure 6 shows the observed ice thickness distribution using ATM 50 m footprints and 50 m PSR derived snow depths [solid line], the distribution produced using full-resolution PSR snow depths averaged to 12.5 km but using the dynamically varying freeboard and snow depth method discussed in Section 4.1 [dotted and dashed line], the distribution produced using the same mean snow depth value for all altimeter measurements (with the condition that the snow depth can not be greater than the measured snow-ice freeboard) [dashed line], and the distribution produced using the snow distribution method used by *Kwok and Cunningham* [2008] (a sigmoidal, rather than linear function for points less than fb_{cutoff}, and a constant $fb_{cutoff} = 1.3H_s$) [dotted line]. In this comparison using the 50 m PSR data is considered the truth or observed because we have a coincident snow depth value for each altimeter

measurement. The figure demonstrates that the snow depth distribution method using a dynamically varying fb_{cutoff} performs well in reproducing the sea ice thickness distribution with the March 22nd region showing particularly good agreement. The largest difference is in the March 21st data set where the method gives a frequency of occurrence 1.6% higher than the observed value for ice with thickness values between 60 cm and 90 cm. The difference between the observed and simulated occurrence frequency for all other ice thickness categories in both the March 21st and March 22nd data sets was less than 1%. Figure 6(c) shows the cumulative probability distributions for the data sets, with the smallest maximum difference (0.01 for both March 21 and March 22) seen with the dynamically varying fb_{cutoff} method.

Using a constant snow depth for every point leads to an overestimate of the amount of thin ice. For greater ice thicknesses (> 200 cm) differences between the approaches are small. The point at which the methods converge is after the freeboard cutoff values of equation (13) and we can see that we are justified in assuming a constant snow depth beyond this cutoff value. The constant freeboard-snow depth method of *Kwok and Cunningham* [2008] has a tendency similar to the constant snow depth method to overestimate the amount of thin ice. This can also be seen in Figure 6(c) with the cumulative probability showing a higher value than the observed value for ice thicknesses less than 100 cm. Dynamically varying the freeboard cutoff value using the method of Section 4.1 gives the smallest deviation from the observed ice thickness distribution compared to the constant snow and constant freeboard-snow depth methods.

5 Impact of ice thickness retrieval resolution on heat flux and ice growth

Sections 3 and 4 have shown that large-scale mean snow depth values (derived from e.g. satellite data) can be combined with high resolution laser altimetry data to obtain the sea ice thickness at the full resolution of ICESat. In this section, we apply the results of the previous sections to satellite data in order to derive basin-wide sea ice thickness values for the Arctic during two separate ICESat measurement campaigns. The impact of the spatial resolution of the derived ice thickness values on energy transport over the ice is then explored to show differences which arise due to the non-linear relationship between ice thickness and heat transport.

5.1 Arctic sea ice thickness values and distribution comparisons

To derive the sea ice thickness of Arctic sea ice we combine ICESat freeboard data with two large-scale snow depth data sets. Snow-ice freeboard is derived from ICESat laser altimetry data (*Zwally et al.*, 2003) using the method of *Kwok et al.* [2007]. The ICESat freeboard retrieval algorithm provides snow-ice freeboard values every 172 m over 25 km segments centered around each sea surface reference point. Snow depth over first year sea ice is derived from the daily microwave brightness temperatures obtained from AMSR-E (*Cavalieri et al.*, 2004) using the algorithm of *Markus and Cavalieri* [1998]. Climatological snow depth values taken from *Warren et al.* [1999] are used for multi-year ice areas.

The snow depth data sets were re-gridded to a polar stereographic grid with a cell size of 25 km to be compatible with the ICESat retrieval length scale. A threshold of 72 ICESat

measurements (equivalent to a 12.5 km line of data) was required for derivation of the ice thickness within each grid cell. The ice and snow thickness values were then estimated at two different spatial resolutions. The low resolution data consists of the 25 km mean snow depth and sea ice thickness values which were calculated using equation (9). The high resolution data consists of an ice and snow thickness value for each ICESat data point. The high resolution data were calculated using the 25 km mean snow depth, 70 m resolution ICESat snow-ice freeboard values, and the methodology described in Section 4 to estimate the snow depth and calculate an ice thickness value for each ICESat data point.

Maps of the snow and ice thickness fields are shown in Figure 7. These can be compared to the snow and ice thickness maps of *Kwok and Cunningham* [2008] who present data from the same ICESat campaigns. Differences in the derived ice thickness values are mainly due to differences in the derived snow depth and freeboard fields. *Kwok and Cunningham* [2008] added a correction term to the freeboard retrieval method of *Kwok et al.* [2007] to account for biases due to the presence of snow within assumed sea surface tie points. Thus, the basin-wide freeboard and ice thickness values used here are expected to be underestimated.

Differences in the spatial structure of the snow depth fields are evident mostly in the multiyear ice area during the February-March 2006 time period. The snow depth climatology of *Warren et al.* [1999] shows little variability in the snow thickness fields during this time period while the fields shown in *Kwok and Cunningham* [2008] have a much higher amount of variability. Additionally, the maximum of the climatological snow depth fields during this time is 40 cm (found only in a small region around the Fram Strait), whereas *Kwok and Cunningham* [2008] find a large fraction of the multiyear ice has a snow thickness greater than 40 cm. However, similarities in the overall spatial structure of the snow and ice thickness

values can be seen. The ice and snow are thickest off Greenland and the Canadian Archipelago with decreasing thickness values towards Siberia. The snow depth fields presented here and in *Kwok and Cunningham* [2008] both show a separation in values between the seasonal and multiyear ice areas. This is expected because the snow cover of the multiyear ice areas can survive the summer melting season and the greater age of the multiyear ice areas means it can experience more snowfall events.

Results of the thickness distributions for October-November, 2005 and February-March, 2006 can be seen in Figure 8. The distributions show the expected growth of the thin ice in the fall to thicker values at the end of the winter with higher percentages of thick ice present. There are differences in the shapes of the distributions for the February-March 2006 period, with the high resolution data showing a greater percentage of thin ice than the low resolution data. This is not unexpected, Figure 6 as well as ice thickness distribution data from other sources (e.g. *Wadhams*, 1981; *Thorndike*, 1975) show that ice thickness distributions tend to be positively skewed so that the amount of thin ice in the Arctic is not reflected in the distribution of the 25 km mean values (low resolution data).

5.2 Heat flux calculations over Arctic sea ice

Using the snow depth and ice thickness maps from the previous section we investigate the effect of the observed values on ocean to atmosphere heat exchange over Arctic sea ice. In addition to the ice thickness and snow depth, the heat exchange depends on variable quantities such as the air temperature, wind speed, and the longwave and shortwave radiation fluxes. We calculate the heat exchange by taking all but the ice thickness and snow depth as constants in order to focus on ice thickness and snow depth effects only. The ocean to atmosphere heat

exchange can be found by solving the energy balance equation over the snow and ice, which can be written as follows (Maykut, *1978*)

$$(1-\alpha)\,F_r + F_L - F_E + F_s + F_c + F_e = 0 \tag{16}$$

where α is the surface albedo, F_r the incoming shortwave flux, F_L the incoming longwave flux, F_E the emitted longwave flux, F_s the sensible heat flux, F_e the latent heat flux, and F_c the conductive heat flux. A positive flux is defined as being toward the surface while a negative flux is away from the surface.

The incoming shortwave flux, F_r, is set to 0 since little to no incoming shortwave radiation is generally available during the late fall and winter time periods for which the snow depth and ice thickness maps were made.

The outgoing longwave radiation is given by

$$F_E = \epsilon\sigma T_0^4 \tag{17}$$

where ϵ is the longwave emissivity of the surface taken to be 0.99, σ is the Stefan-Boltzmann constant, and T_0 is the as yet unknown surface temperature. The downwelling longwave flux is taken to be a constant value of 160 $W\,m^{-2}$. This value comes from an assumed cloud fraction of 80% and the results of *Maykut and Church*, [1973].

The sensible heat flux is given by (*Maykut*, 1978)

$$F_s = \rho c_p C_s u\,(T_a - T_0) \tag{18}$$

where ρ is the average air density (1.3 $kg\,m^{-3}$), c_p is the specific heat of air at constant pressure (1004 $J\,K^{-1}\,kg^{-1}$), u the wind speed, and C_s the sensible heat transfer coefficient taken to be 2×10^{-3}. An air temperature T_a of -20 C, and wind speed u of 10 $m\,s^{-1}$ were used to represent typical Arctic conditions.

The conductive heat flux for snow covered ice is given by (Maykut, *1978*)

$$F_c = \gamma\,(T_b - T_0) \tag{19}$$

where T_b is the temperature at the bottom of the ice taken to be -1.8 C and γ is the thermal conductance of the combined snow and ice system. $\gamma = k_i k_s / (k_s h_i + k_i h_s)$ where h_i and h_s are the ice and snow thicknesses, k_i and k_s are the thermal conductivities of ice and snow which are taken to be 2.04 $W\ m^{-1}K^{-1}$ and 0.31 $W\ m^{-1}K^{-1}$, respectively.

For an air temperature of -20 C the latent heat flux will be of the same sign as the sensible heat flux, however the contribution of the latent heat flux will be much smaller than the range of uncertainty of the sensible heat transfer coefficient for the sensible heat flux (*Pease*, 1987). Therefore, the latent heat flux, F_e, is neglected in the following calculations.

The energy balance equation (16) can then be rewritten using (17), (18), and (19) as

$$\epsilon\sigma T_0^4 + (\rho c_p C_s u + \gamma)\,T_0 - F_L - \rho c_p C_s u T_a - \gamma T_b = 0 \tag{20}$$

The unknown surface temperature, T_0, can be found from equation (20) using Laguerre's method (*Press et al.*, 1992). With the surface temperature known, the ocean to atmosphere heat exchange can be calculated.

The net heat loss to the atmosphere for the ice covered regions ($-F_c$) is shown in Figure

9 using the observed ice and snow thickness distributions for the late fall and winter time periods then gridded to a 25 km polar stereographic grid. Also shown is the heat loss calculated using large-scale 25 km mean snow and ice thickness values. The average heat loss calculated from the full resolution ice and snow thickness distribution data sets is higher by 7.6 $W\ m^{-2}$ (37%) and 5.2 $W\ m^{-2}$ (33%) for the October-November 2005 and February-March 2006 time periods, respectively. The results show much larger heat flux values over the younger and thinner first-year ice cover compared to the multiyear ice region, with only small heat flux values seen over the multiyear ice region. The late winter heat flux values show a reduction over the late fall season values due to the growth of the ice and addition of more snow reducing the thermal conductivity of the system. Differences between the heat fluxes calculated by considering the full distribution of ice and snow thicknesses as opposed to the large-scale mean values are more pronounced over the first-year ice regions, with only small differences over the thicker multiyear ice regions. This is in contrast to *Maykut* [1978] who predicts larger differences between the methods for the central Arctic. The main reason for this difference is due to the different distributions of snow cover used. *Maykut* [1978] assumes no snow cover on ice less than 0.8 m thick while we assume a layer of variable snow depth on ice of all thicknesses.

In addition to the heat fluxes, the basal ice growth rate $\frac{dh_i}{dt}$ can also be calculated and is given by

$$\frac{dh_i}{dt} = \frac{1}{Q_I}\left[\frac{k_i}{h_i}\left(T_b - T_i\right) - F\uparrow\right] \tag{21}$$

where Q_I is the heat of fusion of ice taken to be 302 $MJ\ m^{-3}$, $F\uparrow$ is the oceanic heat flux

taken to be 2 $W\ m^{-2}$, and T_i is the ice surface temperature equal to $(T_0 + \zeta T_b) / (1 + \zeta)$ where $\zeta = k_i h_s / k_s h_i$ (*Parkinson and Washington*, 1979). Ice growth rates are shown in Figure 10 for the late fall and winter time periods. The results show much more vigorous ice production in the first year ice areas during the late fall with little growth occurring in multiyear ice and during the late winter time period. Differences between the ice growth rates calculated by considering the full distribution of ice and snow thicknesses as opposed to the large-scale mean values are mainly significant over first year ice areas during the late fall season. This is due to the non-linear dependence of the heat flux on ice and snow thickness and the higher amounts of thin ice observed in the first year ice areas. Using the full resolution ice and snow thickness distribution gives a greater amount of heat exchange with the atmosphere leading to a higher ice growth rate than would be predicted using the large-scale mean values. The average growth rates calculated from the full resolution data are higher by 0.21 $cm\,day^{-1}$ (39%) and 0.15 $cm\,day^{-1}$ (38%) for the October-November 2005 and February-March 2006 time periods, respectively.

Integrating the ice growth rate over the 4 month time period between the October-November 2005 and February-March 2006 ice thickness measurements would give the total increase in ice thickness due to basal growth. Although the ice growth rate as a function of time is not known, to first order we can approximate the growth rate over the 4 month time period by taking it to vary as a linear function of time. This assumption of a linear change in the growth rate will overestimate the actual basal ice growth because of the nonlinear dependence of the growth rate on ice thickness. However, the purpose of the exercise is to place the differences in the calculated heat exchange into a more familiar number, a difference in mean ice thickness over a 4 month growing season. Additionally, since it is necessary

to know the ice growth rate at the beginning and ending time points, the integration can only be performed where there is coincident data in both the October-November 2005 and February-March 2006 time periods. By using these conditions, we find a difference of 18 cm in the ice thickness over a 4 month time period using the different basal ice growth rates calculated from the high and low resolution data.

6 Summary and Discussion

The main focus of this study is to address the spatial resolution of the estimated sea ice thickness values and uncertainties that result from the combination of satellite derived freeboard and snow depth values. However, further work needs to be done to better understand the error in the derived ice thickness value due to the density variations of snow and ice, uncertainties in the snow depth and altimetry data, and the assumption that the hydrostatic balance equation holds over the altimeter footprint. Large differences were observed in the spatial structure of the snow depth fields from the climatology of *Warren et al.* [1999] used here and the snow depth fields of *Kwok and Cunningham* [2008] which were estimated from ECMWF snowfall data. There are numerous possible reasons for the observed differences (e.g. the climatology was developed over the period 1954-1991 and may not reflect present conditions). Nonetheless, validation and estimation of uncertainties in the snow depth fields are critically needed. Despite the various uncertainties, *Kwok and Cunningham* [2008] found agreement to within 0.5 m between estimates of ice draft from two ICESat campaigns and moorings in the Beaufort Sea. The assumption that the hydrostatic balance equation is valid over the altimeter footprint may not hold since an ice floe is a rigid body, thus hydrostatic

equilibrium is not necessarily achieved at every point. A free floating ice floe is assumed to cover the footprint area for the data sets used here, but the validity of this assumption awaits further study.

Using high resolution aircraft data we have studied the magnitude of the errors expected to be encountered in using a large-scale snow depth grid cell value as an estimate of the mean snow depth encountered along a coincident altimeter track. The scales of these error estimates ranged from an AMSR-E snow depth grid cell to larger sized model snow depth grid cells. The uncertainty in snow depth along the altimeter track is shown to be a function of the snow depth retrieval uncertainty and the spatial variability of snow within the large-scale snow depth grid cell. An estimate for the snow depth uncertainty due to spatial variability was found to be 13% of the large-scale snow depth grid cell value. The propagation of the error due to spatial variability of snow into the derived ice thickness value was found to be comparable to or smaller than the contributions from uncertainties in the retrieval of the freeboard and snow depth.

Using the assumption that the snow depth along the altimeter track is well represented by a large-scale snow depth grid cell value, we have developed a method to bring the snow depth from the large-scale resolution of a snow depth grid cell to the scale of the altimetry measurement. This allows for the derivation of the sea ice thickness distribution on the spatial scale of laser altimetry measurements. The method is based on high resolution aircraft observations showing a correlation between freeboard and snow depth for points with a freeboard less than a certain freeboard cutoff value. The cutoff value was found to depend on the mean freeboard and snow depth of an area, a regression of visually derived freeboard cutoff values provides a method to estimate the cutoff value with an uncertainty of 4.4

cm. Snow depth values for points with freeboards above the cutoff value were found to be randomly distributed around a common mean which is found by requiring the snow depth along the altimeter track to be equal to the snow depth of the large-scale grid cell value. Given input that simulates current large-scale satellite measurements, the method is able to satisfactorily estimate the sea ice thickness distributions of the high resolution aircraft data sets for two areas. These areas were chosen to represent two distinct first-year ice snow regimes as observed in AMSR-E data. The maximum difference between the observed and reproduced occurrence frequencies is 1.6% with a maximum cumulative probability difference of 0.01.

Freeboard is the only laser altimetry data product used in our approach, but the inclusion of more variables available from altimetry data such as surface roughness and reflectivity could potentially be used to enhance the results further. Reflectivity data could be used to identify snow-free areas of ice because of the large difference in albedo between ice and snow at the 1064 nm wavelength used by ICESat (*Wiscombe and Warren*, 1980). Surface roughness data could be used to identify ridged or rubbled areas which may have a higher snow depth than the surrounding area due to the tendency of wind-blown snow to be preferentially trapped in these regions (*Sturm et al.*, 2006).

Heat exchange over the sea ice has been studied for cases typical of late fall to winter conditions in the Arctic using ice and snow thickness distributions estimated from satellite data. Using the high resolution snow and ice thickness data was found to give a greater loss of heat from the ocean to the atmosphere leading to approximately one third higher thermodynamic ice growth rates and ocean to atmosphere heat losses when compared to values derived from large-scale 25 km mean values of ice and snow thickness. Using the high

resolution ice and snow thickness distributions for the October-November 2005 time period gives an average heat flux 7.6 $W\,m^{-2}$ (37%) and ice growth rate 0.21 $cm\,day^{-1}$(39%) higher than the respective values calculated using the large-scale 25 km mean. Similarly, data for the February-March 2006 time period gives an average heat flux 5.2 $W\,m^{-2}$ (33%) and ice growth rate 0.15 $cm\,day^{-1}$ (38%) higher than the respective values calculated from the large-scale 25 km mean.

The cumulative effect of the difference in ice growth rates between the high and low resolution methods was estimated to lead to an 18 cm difference in basal ice growth over a 4 month time period. Estimates of the actual basal ice growth over this time period are not known, however, due to the limited sampling of the ice thickness to periods when ICESat is switched on. Continuous sampling of the ice cover by future altimetry missions such as ICESat-2 could be used to better understand this process. Furthermore, the use of observed air temperature, wind speed, and longwave flux values (e.g. from NCEP-NCAR reanalysis data [*Kalnay et al.*, 1996]) could be used to better estimate the cumulative impact of the ocean-ice-atmosphere heat exchange process over the observed time periods.

7 Conclusion

In this study we have discussed some of the major issues encountered in the estimation of sea ice thickness from combinations of satellite freeboard and snow depth data sets. These issues arise because of the large difference in spatial resolution and coverage between the snow depth and freeboard data sets. The differences introduce errors into the derived ice thickness value as well as ambiguities in the resolution with which to derive the sea ice thickness.

Current research using combinations of ICESat laser altimetry and snow depth data has been focused on the estimation and validation of kilometer-scale ice thickness values (e.g. *Kwok and Cunningham,* 2008; *Zwally et al.,* 2008). Knowledge of the sea ice thickness at kilometer scales is needed to understand the state of the sea ice system, while observations over multiple years will be useful for understanding changes that are occurring in the system. The present study demonstrates the ability of satellite measurements to be used to estimate the sea ice thickness distribution of an area with the high spatial resolution of a laser altimeter (~70 m for ICESat). Geophysically important parameters such as the heat flux, air/water stress, and ice strength depend on the ice and snow thickness distributions at this scale. These parameters in turn affect large-scale climate parameters such as the oceanic and atmospheric circulations. The availability of Arctic basin-wide ice and snow thickness distributions should thus be of benefit to understanding the impact of the climate on the sea ice system, and the impact of sea ice on the climate.

8 Acknowledgments

The authors would like to thank the mission and flight crew for their invaluable contributions to the AMSR-E 2006 campaign. We would also like to thank the associate editor and two anonymous reviewers for their thorough reading of the manuscript and their constructive comments and suggestions.

This work has been supported through NASA's Cryosphere Program.

9 References

Cavalieri, D.J. and T. Markus, EOS Aqua AMSR-E Arctic sea ice validation program: Arctic 2006 aircraft campaign flight report, *NASA/TM-2006-214142*, 27 pp., 2006.

Cavalieri, D.J., T. Markus, and J.C. Comiso. 2004, updated daily. *AMSR-E/Aqua Daily L3 12.5 km Brightness Temperature, Sea Ice Conentration, & Snow Depth Polar Grids B06*, October-November 2005 and February-March 2006. Boulder, Colorado USA: National Snow and Ice Data Center. Digital media.

Comiso, J.C., D.J. Cavalieri, and T. Markus, Sea ice concentration, ice temperature, and snow depth using AMSR-E data, *IEEE Transactions on Geoscience and Remote Sensing*, vol.41, no.2, pp. 243-252, Feb. 2003.

Curry, J.A., J.L. Schramm, and E.E. Ebert, Sea ice-albedo climate feedback mechanism, *J. Climate,* vol. 8, pp. 240-247, 1995.

Egbert, G.D., and L. Erofeeva, Efficient inverse modeling of barotropic ocean tides, *Journal of Atmospheric and Oceanic Technology*, vol.19, N2, 2002.

Farrell, S.L., S.W. Laxon, D.C. McAdoo, D. Yi, and H. J. Zwally, Five years of Arctic sea ice freeboard measurements from the Ice, Cloud and land Elevation Satellite, *J. Geophys Res.*, vol. 114, C04008, doi:10.1029/2008JC005074, 2009.

Forsberg, R., and H. Skourup, Arctic Ocean gravity, geoid, and sea-ice freeboard heights from ICESat and GRACE, *Geophys. Res. Lett., 32*, L21502, doi:10.1029/2005GL023711, 2005.

Holland, M.M., C.M. Bitz, E.C. Hunke, W.H. Lipscomb, J.L. Schramm, Influence of the sea ice thickness distribution on polar climate in CCSM3, *J. Climate*, vol. 19, 2006.

Kalnay, E., M. Kanamitsu, R. Kistler, W. Collins, D. Deaven, L. Gandin, M. Iredell, S. Saha, G. White, J. Woollen, Y. Zhu, A. Leetmaa, R. Reynolds, M. Chelliah, W. Ebisuzaki, W. Higgins, J. Janowiak, K. C. Mo, C. Ropelewski, J. Wang, R. Jenne, and D. Joseph, The NCEP/NCAR 40-year reanalysis project, *Bull. Amer. Meteor. Soc., 77*, 437-470, 1996.

Kenyon, S., and R. Forsberg, Arctic Gravity Project: A status, in Gravity, Geoid and Geodynamics 2000, Int. Assoc. Geod. Symp., vol. 123, edited by M. G. Sideris, pp. 391-395, Springer, New York., 2001.

Kovacs, A., Sea ice: Part II. Estimating the full-scale tensile, flexural, and compressive strength of first-year ice, *CRREL Rep. 96-11*, Cold Reg. Res. and Eng Lab., Hanover, NH, 1996.

Krabill, W.B., R.H. Thomas, C.F. Martin, R.N. Swift, and E.B. Frederick, Accuracy of airborne laser altimetry over the Greenland ice sheet, I*nt. J. Rem. Sens., 16*, 1211-1222, 1995.

Kurtz, N.T., T. Markus, D.J. Cavalieri, W.B. Krabill, J.G. Sonntag, and J. Miller, Comparison of ICESat Data With Airborne Laser Altimeter Measurements Over Arctic Sea Ice, *IEEE Transactions on Geoscience and Remote Sensing*, vol.46, no.7, pp.1913-1924, July 2008.

Kwok, R. G.F. Cunningham, H.J. Zwally, and D. Yi, ICESat over Arctic sea ice: Retrieval of freeboard, *J. Geophys. Res.*, vol. 112, C12013, Dec. 2007. DOI: 10.1029/2006JC003978.

Kwok, R. and G.F. Cunningham, ICESat over Arctic sea ice: Estimation of snow depth and ice thickness, *J. Geophys. Res.*, vol. 113, C08010, 2008. DOI: 10.1029/2008JC004753.

Laxon, S., N. Peacock, and D. Smith, High interannual variability of sea ice thickness in the Arctic region, *Nature, 425*, pp. 947-950, 2003.

Maksym, T., and T. Markus, Antarctic sea ice thickness and snow-to-ice conversion from

atmospheric reanalysis and passive microwave snow depth, *J. Geophys. Res.*, vol. 113, C02S12, 2008. DOI:10.1029/2006JC004085.

Markus, T. and D.J. Cavalieri, Snow depth distribution over sea ice in the Southern Ocean from satellite passive microwave data, in *Antarctic Sea Ice Physical Processes, Interactions and Variability, Antarctic Research Series, 74*, edited by M.O. Jeffries, pp.19-40, AGU, Washington, D.C., 1998.

Massom, R.A., Drinkwater, M.R., and C. Haas, Winter snow cover on sea ice in the Weddell Sea, *J. Geophys. Res.*, vol. 102, 1101-1117, 1997.

Maykut, G.A., Energy exchange over young sea ice in the central Arctic, *J. Geophys. Res.*, vol. 83, pp.3646-3658, 1978.

Maykut, G.A. and P.E. Church, Radiation climate of Barrow, Alaska, 1962-66, *J. Appl. Meteorol.*, 12(4), 620-628, 1973.

Parkinson, C.L., and W.M. Washington, A large-scale numerical model of sea ice, *J. Geophys. Res.*, vol. 84, pp.311-337, 1979.

Peacock, N.R. and S.W. Laxon, Sea surface height determination in the Arctic Ocean from ERS altimetry. *J. Geophys. Res.*, vol. 109, C07001, 2004.

Pease, C.H., The size of wind-driven coastal polynyas, *J. Geophys. Res.*, vol. 92, pp.7049-7059, 1987.

Percival, D.B., D.A. Rothrock, A.S. Thorndike, and T. Gneiting, The variance of mean sea-ice thickness: Effect of long-range dependence, *J. Geophys. Res.*, vol. 113, C01004, 2008. DOI:10.1029/2007JC004391.

Piepmeier, J.R., and A.J. Gasiewski, Polarimetric scanning radiometer for airborne microwave imaging studies, *Geoscience and Remote Sensing Symposium, 1996. IGARSS '96.*

'International Remote Sensing for a Sustainable Future.', vol.2, no., pp.1120-1122 vol.2, 27-31 May 1996.

Press, W. H., B.P. Flannery, S.A. Teukolsky, and W.T. Vetterling, Numerical Recipes in FORTRAN: The Art of Scientific Computing, 2nd ed. Cambridge, England: Cambridge University Press, pp. 365-366, 1992.

Rothrock, D.A., Y. Yu, and G.A. Maykut, Thinning of the Arctic sea-ice cover, *Geophys. Res. Lett., 26*, 3469-3472, 1999.

Spreen, G., S. Kern, D. Stammer, R. Forsberg, and J. Haarpainter, Satellite-based estimates of sea-ice volume flux through Fram Strait, *Ann. Glaciol,* 44, 321-328, 2006.

Sturm, M., and C.S. Benson, Vapor transport, grain growth, and depth hoar development in the sub-Arctic snow, *J. Glaciol.*, vol. 43, pp.42-59, 1997.

Sturm, M., Maslanik, J.A., Perovich, D., Stroeve, J.C., Richter-Menge, J., Markus, T., Holmgren, J., Heinrichs, J.F., Tape, K., Snow depth and ice thickness measurements from the Beaufort and Chukchi Seas collected during the AMSR-Ice03 Campaign, *IEEE Transactions on Geoscience and Remote Sensing, 44*, doi:10.1109/TGRS.2006.878236, 2006.

Thorndike, A.S., D.A. Rothrock, G.A. Maykut, and R. Colony, The thickness distribution of sea ice, *J. Geophys. Res.*, vol. 80, pp.4501-4513, 1975.

Tin, T., and M.O. Jeffries, Sea-ice thickness and roughness in the Ross Sea, Antarctica, *Ann. Glaciol, 33*, 187-193, 2001.

Wadhams, P., Ice thickness in the Arctic Ocean: The statistical reliability of experimental data, *J. Geophys. Res.*, vol. 102(C13), 27,951-27,959, 1997.

Wadhams, P., Sea-ice topography of the Arctic Ocean in the region 70 W to 25 E, *Philosophical Transactions of the Royal Society of London, Series A, Mathematical and Physical*

Sciences, Vol. 302, No. 1464, 45-85, 1981.

Warren, S.G., I.G. Rigor, N. Untersteiner, V.F. Radionov, N.N. Bryazgin, Y.I. Aleksandrov, and R. Colony, Snow depth on Arctic sea ice, *J. Climate*, 12 (6), 1814-1829, 1999.

Wiscombe, W.J., and S.G. Warren, A model for the spectral albedo of snow I: Pure snow, *J. Atmos. Sciences,* vol. 37, 1980.

Zwally, H.J., R. Schutz, C. Bentley, J. Bufton, T. Herring, J. Minster, J. Spinhirne, and R. Thomas. 2003, *GLAS/ICESat L2 Sea Ice Altimetry Data V428*, October-November 2005 and February-March 2006. Boulder, CO: National Snow and Ice Data Center. Digital media.

Zwally, H.J., D. Yi, R. Kwok, and Y. Zhao, ICESat measurements of sea ice freeboard and estimates of sea ice thickness in the Weddell Sea, *J. Geophys. Res.*, *113*, C02S15, doi:10.1029/2007JC004284, 2008.

Zwally, H.J., R. Schutz, W. Abdalati, J. Abshire, C. Bentley, A. Brenner, J. Bufton, J. Dezio, D. Hancock, D. Harding, T. Herring, B. Minster, K. Quinn, S. Palm, J. Spinhirne and R. Thomas, ICESat's laser measurements of polar ice, atmosphere, ocean, and land, *J. Geodyn., 24*, 405-445, 2002.

10 Figure captions

Figure 1. Map of the AMSR-E Arctic sea ice validation campaign aircraft flights in March 2006 made from Fairbanks, AK. The flights on March 18th and 20th near Barrow, AK were for aircraft instrumentation calibaration and validation. The flights on March 21st and 22nd were chosen to represent two distinct types of snow covers over first year sea ice and were used for this study. The March 24th flight was underneath and ICESat orbit while the March 25th flight was over a mixture of first-year and multiyear ice.

Figure 2. A representation of the method used to derive the uncertainty in snow depth along an ICESat altimeter track due to spatial variability. The lighter colored lines are the flight path of the aircraft with associated high resolution freeboard and snow depth values, the dark colored boxes are of the size of a snow depth grid cell from passive microwave or model data. S^i is the mean value along an individual flight track within the larger snow depth grid cell while $< S >$ is the mean value of all of the segments within a snow depth grid cell. The distance between the flight lines is ~ 5 km.

Figure 3. Histogram of the differences between the mean snow depth of a grid cell and the snow depth along an individual flight track within the grid cell (δ as defined by equation 8) for a) the March 21st study area and b) the March 22nd study area. The dashed line is a Gaussian distribution with equivalent mean and standard deviation.

Figure 4. Example plots of snow depth vs. snow-ice freeboard for two 12.5 km transects. The dashed line shows the calculated freeboard cutoff value (fb_{cutoff}) after which snow depth is no longer correlated with snow-ice freeboard. The solid line illustrates our approach to assign different snow depth values to individual altimeter points for small freeboards, and

using an average snow depth only for freeboards greater than the dashed line.

Figure 5. Visually derived freeboard cutoff values compared to the multiple linear regression cutoff.

Figure 6. Ice thickness distributions for observed and simulated freeboard and snow depth conversions to ice thicknesses. a) March 21 study area. b) March 22 study area. c) Cumulative distributions for the March 21 and 22 study areas.

Figure 7. Ice and snow thickness fields derived from the combined ICESat, AMSR-E, and snow climatology data sets. The grey contour line is the extent of the predominantly multiyear ice area.

Figure 8. Ice thickness distributions for the combined ICESat, AMSR-E, and snow climatology data sets. a) The October-November 2005 time period. b) The February-March 2006 time period. c) Cumulative distributions for the two time periods.

Figure 9. Map of the ocean to atmosphere heat flux ($-F_c$) over ice covered regions (excluding the open water contribution) calculated using the snow and ice thickness distributions (high-resolution) and large-scale 25 km gridded mean values (low resolution). The difference between the methods is also plotted. The grey contour line is the extent of the predominantly multiyear ice area. Note that a different color scale is used for the difference plots. Mean values of all grid points for the October-November 2005 time period are 28.3 $W\,m^{-2}$ and 20.7 $W\,m^{-2}$ for the high and low resolution methods, respectively. Mean values of all grid points for the February-March 2006 time period are 20.8 $W\,m^{-2}$ and 15.6 $W\,m^{-2}$ for the high and low resolution methods, respectively.

Figure 10. Map of the thermodynamic ice growth rate of ice covered regions calculated using the snow and ice thickness distributions (high-resolution) and large-scale 25 km gridded

mean values (low resolution). The difference between the methods is also plotted. The grey contour line is the extent of the predominantly multiyear ice area. Note that a different color scale is used for the difference plots. Mean values of all grid points for the October-November 2005 time period are .75 $cm\,day^{-1}$ and .54 $cm\,day^{-1}$ for the high and low resolution methods, respectively. Mean values of all grid points for the February-March 2006 time period are .54 $cm\,day^{-1}$ and .39 $cm\,day^{-1}$ for the high and low resolution methods, respectively.

11 Table captions

Table 1. Observed uncertainty due to spatial variability in the mean snow depth of a simulated ICESat track within a large-scale passive microwave or model snow depth grid cell. The number of grid cells and lines within each grid cell vary due to gaps in the data and the availability of cross track flight lines.

Table 2. Mean values in cm of the total measured data for each study area.

Grid cell size	12.5 km	25 km	50 km
Snow depth uncertainty [cm] (March 21, 22)	2.5, 3.6	2.1, 3.5	2.2, 3.2
Maximum # of grid cells in study area	32	8	2
# of lines within each grid cell (March 21, 22)	3 to 6, 3 to 6	5 to 8, 5 to 9	11, 10

	Snow-ice freeboard	Freeboard	Snow depth
March 21	45.8	26.9	18.9
March 22	46.4	18.7	27.7

2006 Alaska Sea Ice Flights

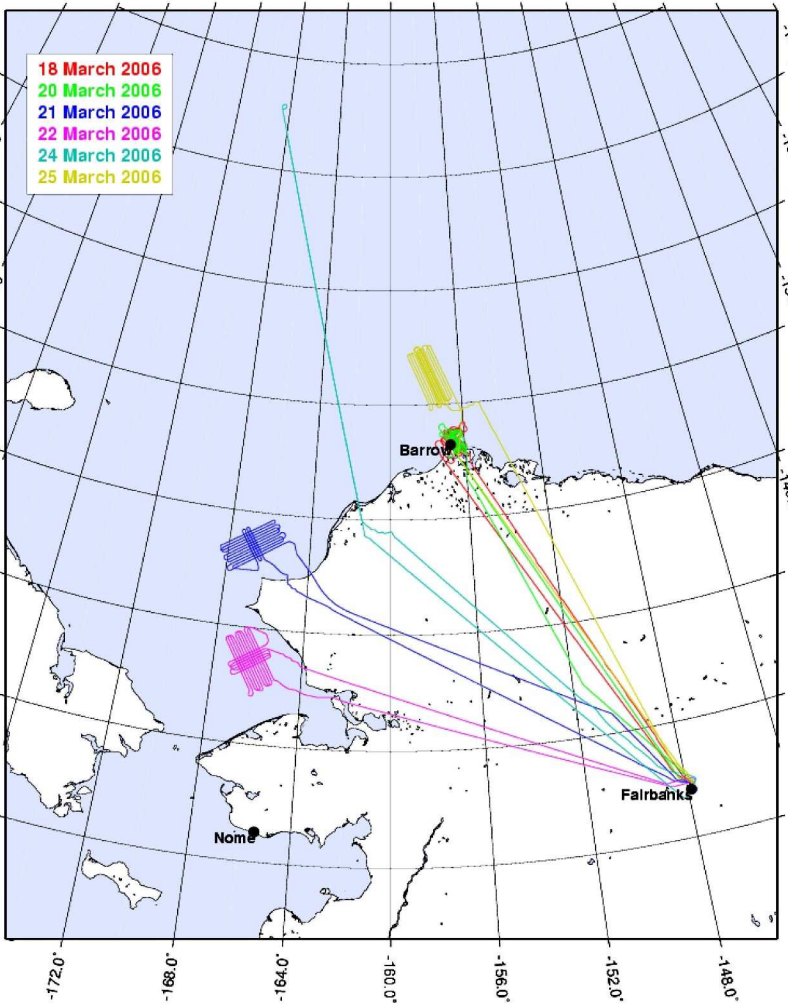

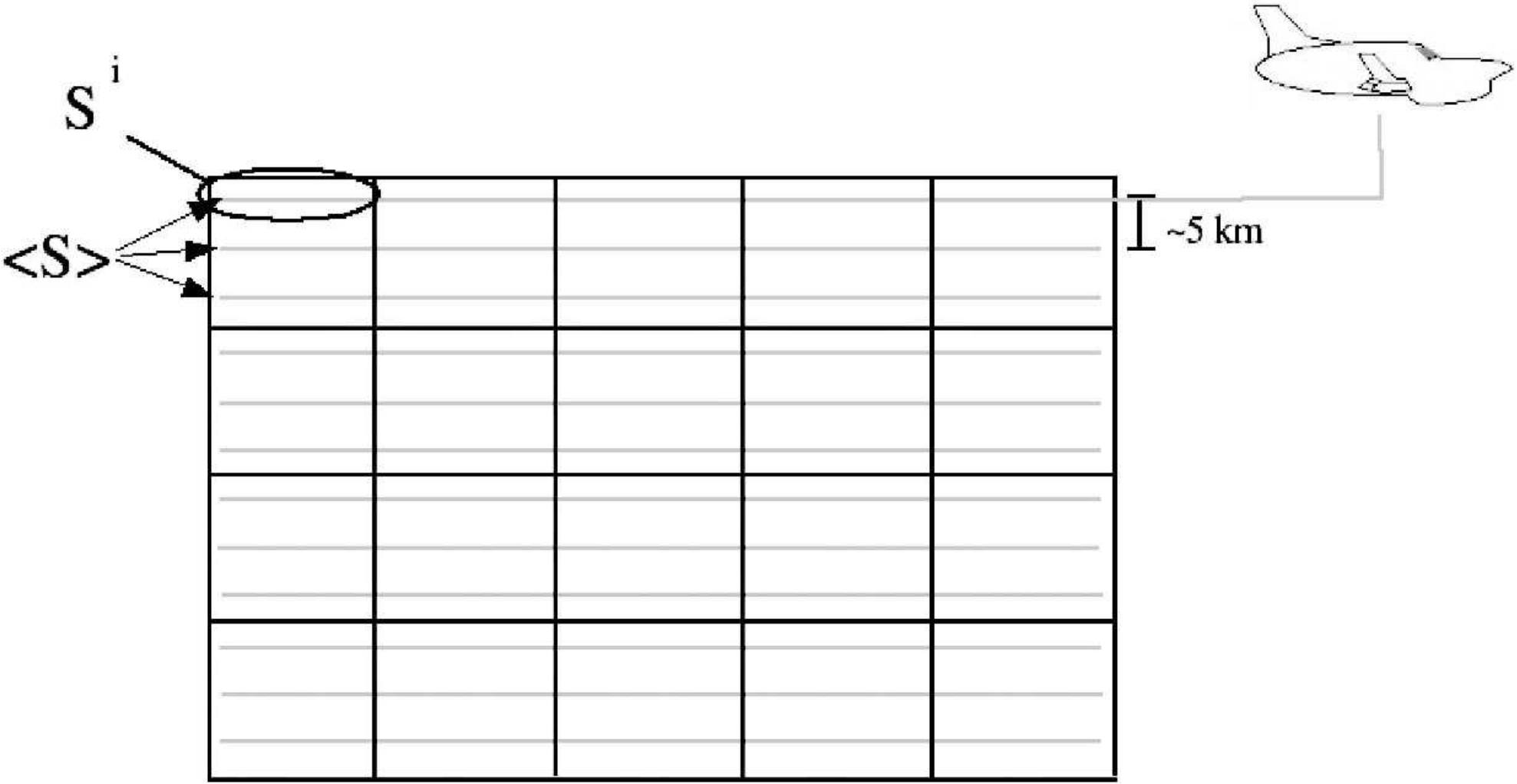
S i
<S>
~5 km

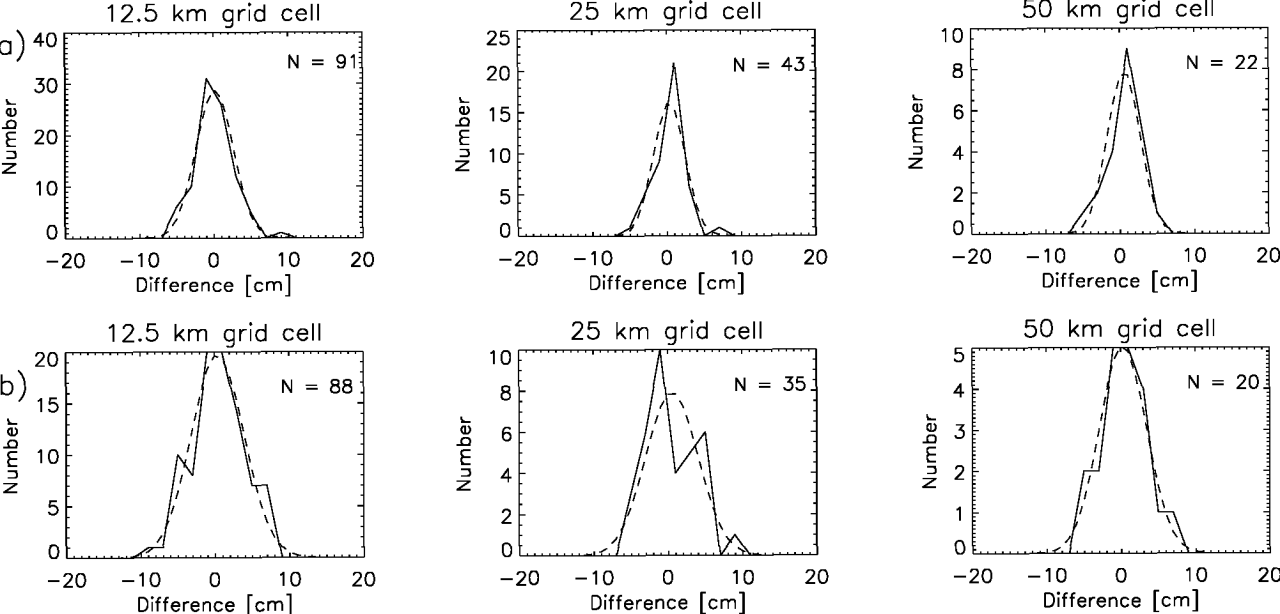
a)
12.5 km grid cell
N = 91
25 km grid cell
N = 43
50 km grid cell
N = 22
b)
12.5 km grid cell
N = 88
25 km grid cell
N = 35
50 km grid cell
N = 20
Number
Difference [cm]

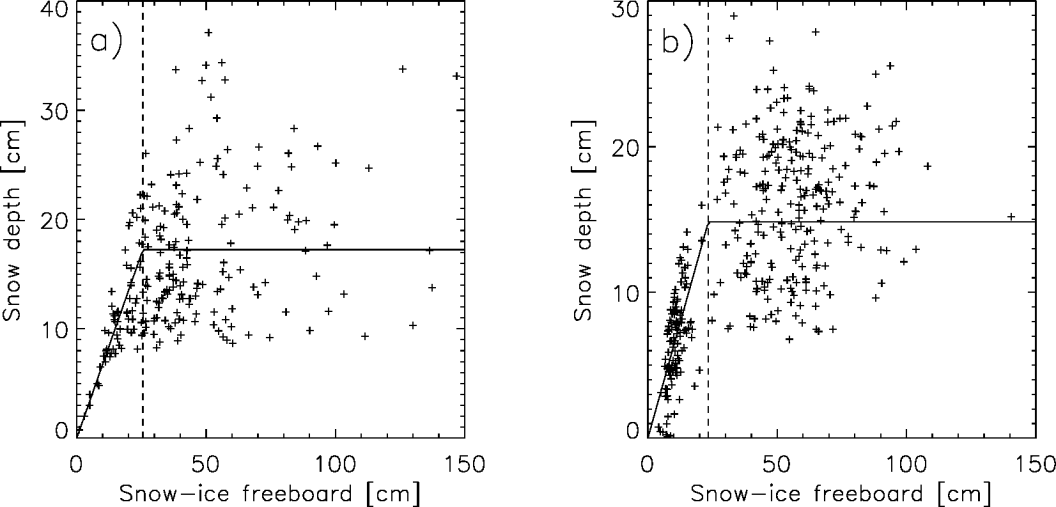
a)
b)
Snow depth [cm]
Snow−ice freeboard [cm]
0
10
20
30
40
50
100
150

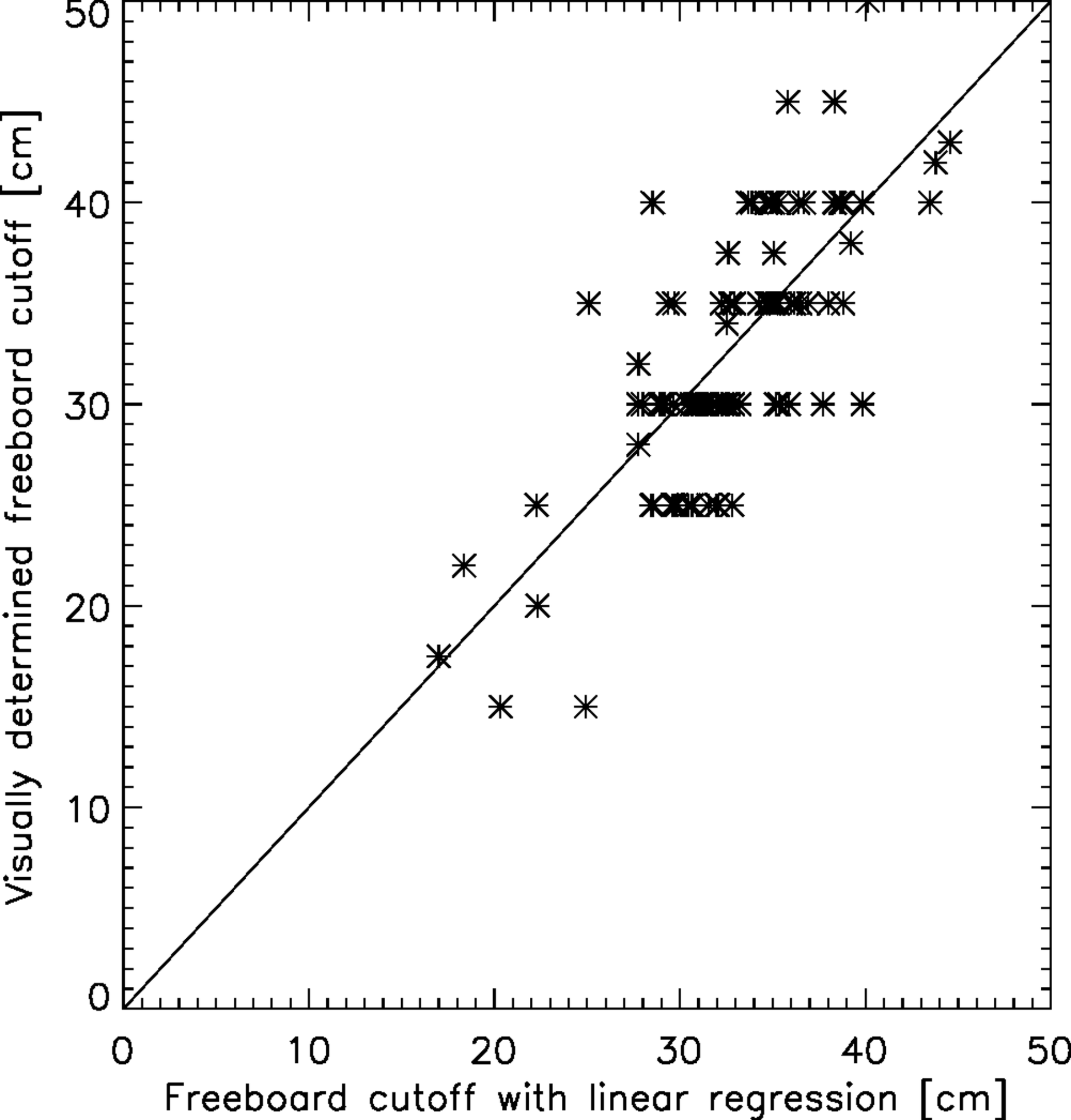
Visually determined freeboard cutoff [cm]
Freeboard cutoff with linear regression [cm]
0
10
20
30
40
50

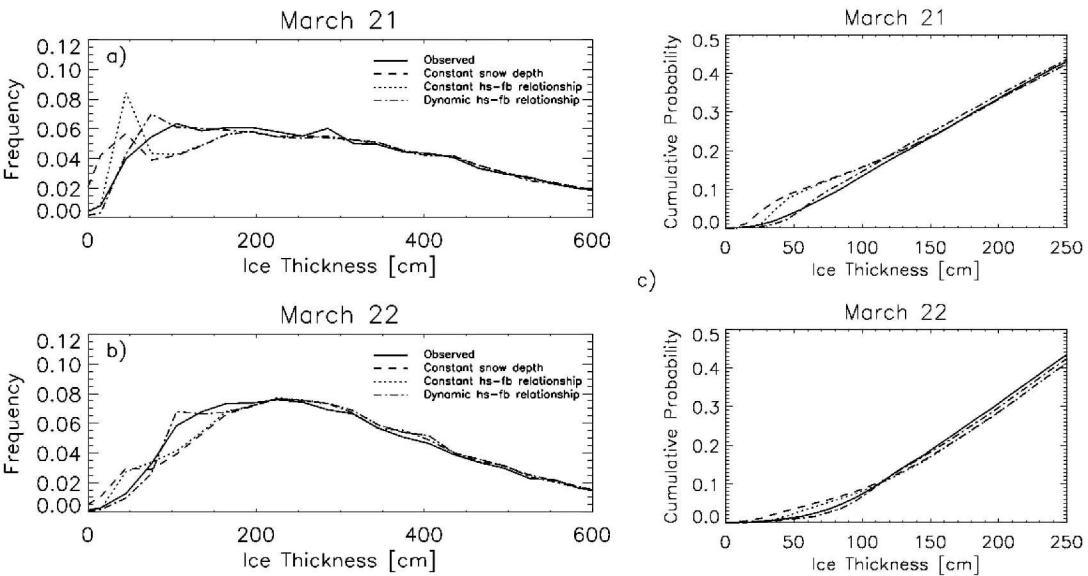
March 21
a)
Observed
Constant snow depth
Constant hs-fb relationship
Dynamic hs-fb relationship
Frequency
Ice Thickness [cm]
March 21
Cumulative Probability
Ice Thickness [cm]
c)
March 22
b)
Observed
Constant snow depth
Constant hs-fb relationship
Dynamic hs-fb relationship
Frequency
Ice Thickness [cm]
March 22
Cumulative Probability
Ice Thickness [cm]

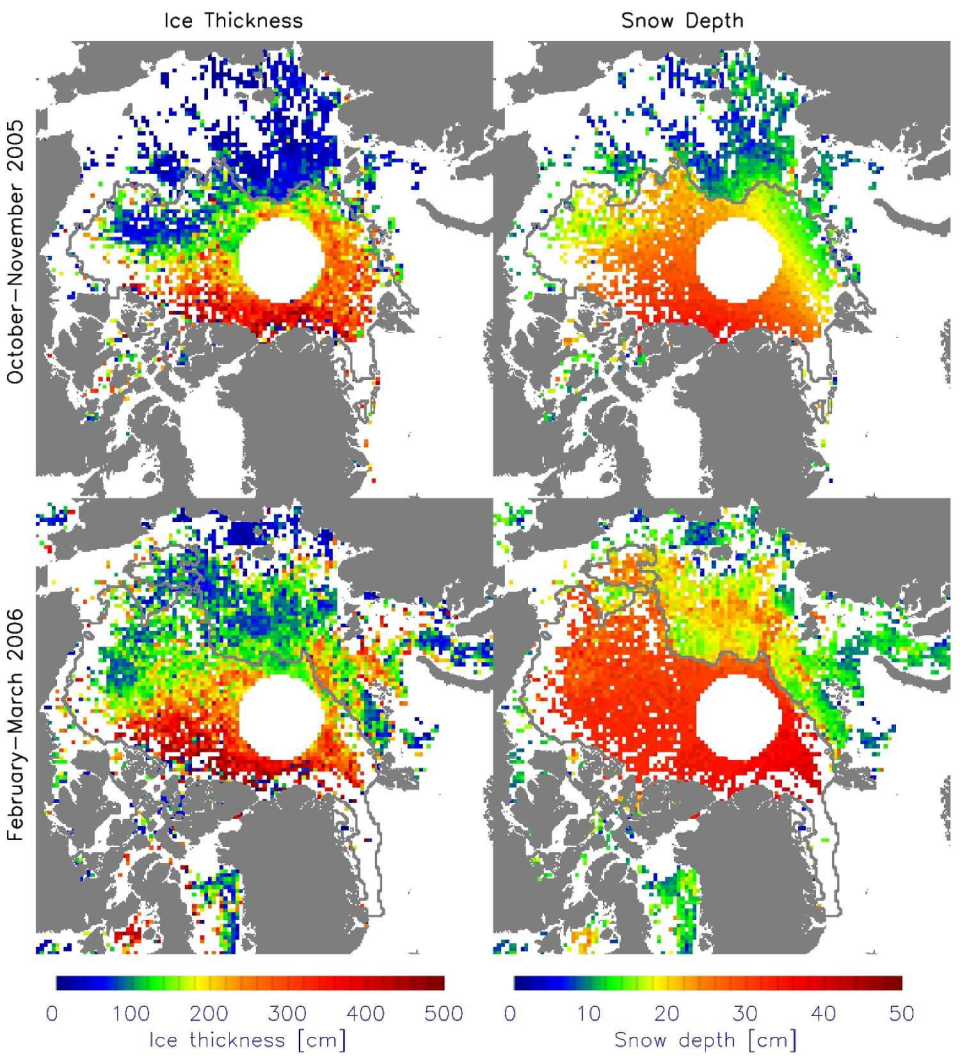
Ice Thickness
Snow Depth
October–November 2005
February–March 2006
0
100
200
300
400
500
Ice thickness [cm]
0
10
20
30
40
50
Snow depth [cm]

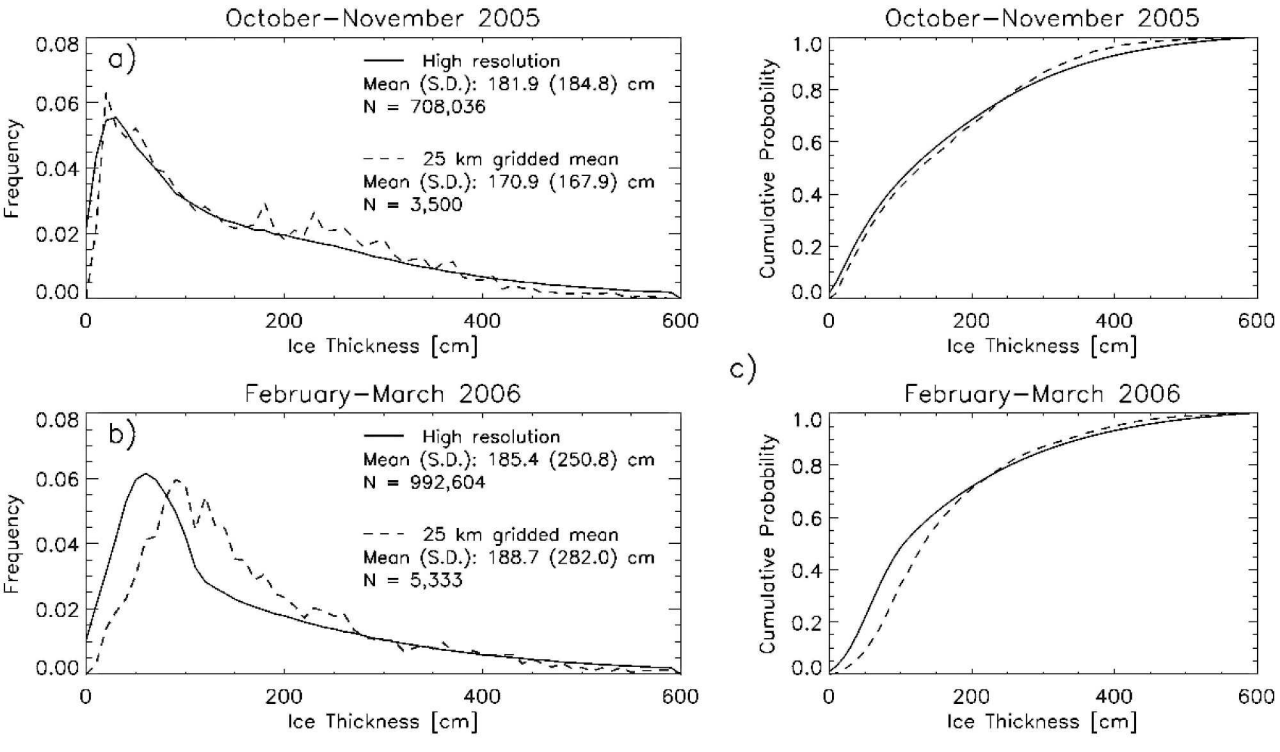
October–November 2005
a)
High resolution
Mean (S.D.): 181.9 (184.8) cm
N = 708,036
25 km gridded mean
Mean (S.D.): 170.9 (167.9) cm
N = 3,500
Frequency
Ice Thickness [cm]
October–November 2005
Cumulative Probability
Ice Thickness [cm]
c)
February–March 2006
b)
High resolution
Mean (S.D.): 185.4 (250.8) cm
N = 992,604
25 km gridded mean
Mean (S.D.): 188.7 (282.0) cm
N = 5,333
Frequency
Ice Thickness [cm]
February–March 2006
Cumulative Probability
Ice Thickness [cm]

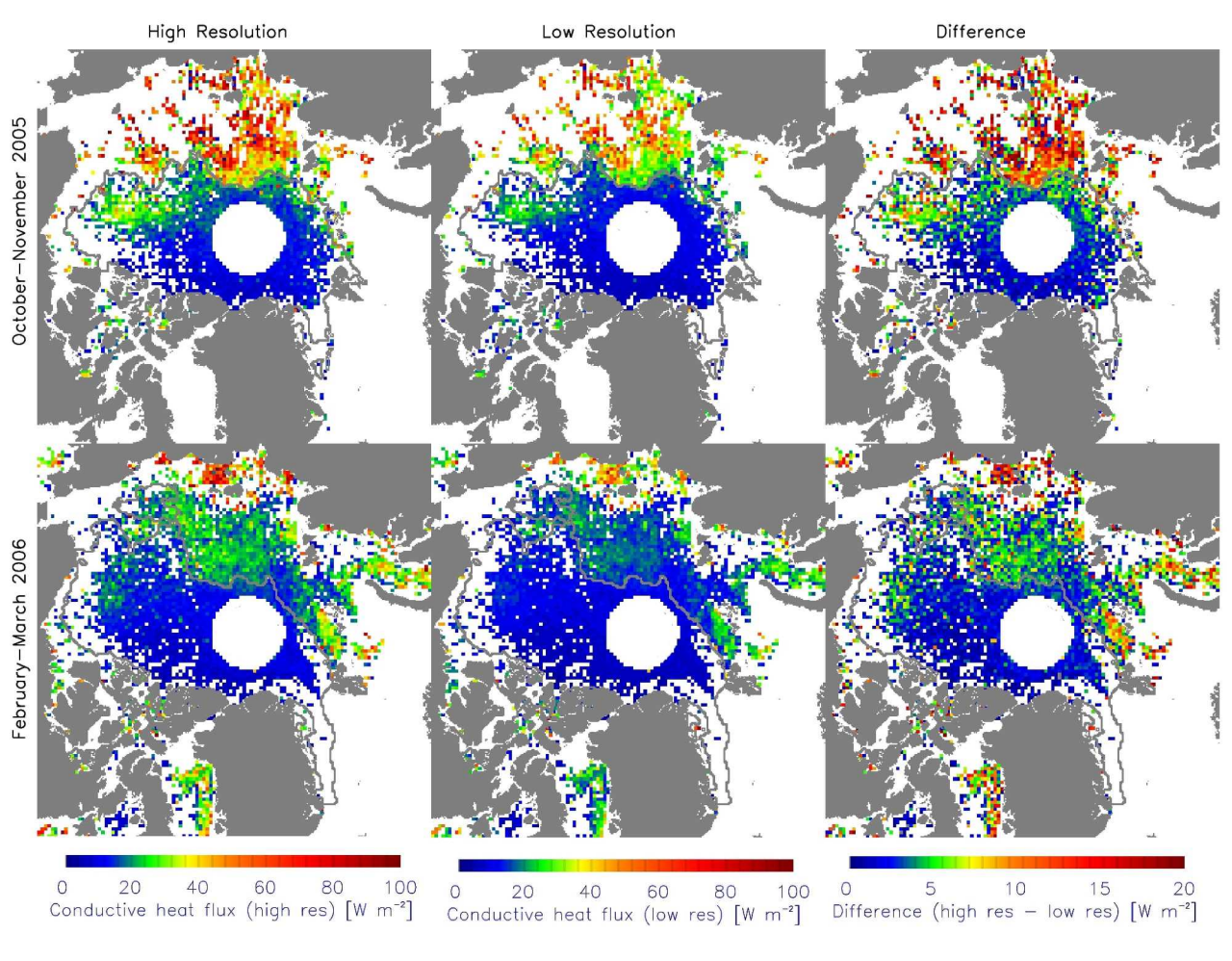
High Resolution
Low Resolution
Difference
October–November 2005
February–March 2006
0 20 40 60 80 100
Conductive heat flux (high res) [W m⁻²]
0 20 40 60 80 100
Conductive heat flux (low res) [W m⁻²]
0 5 10 15 20
Difference (high res – low res) [W m⁻²]

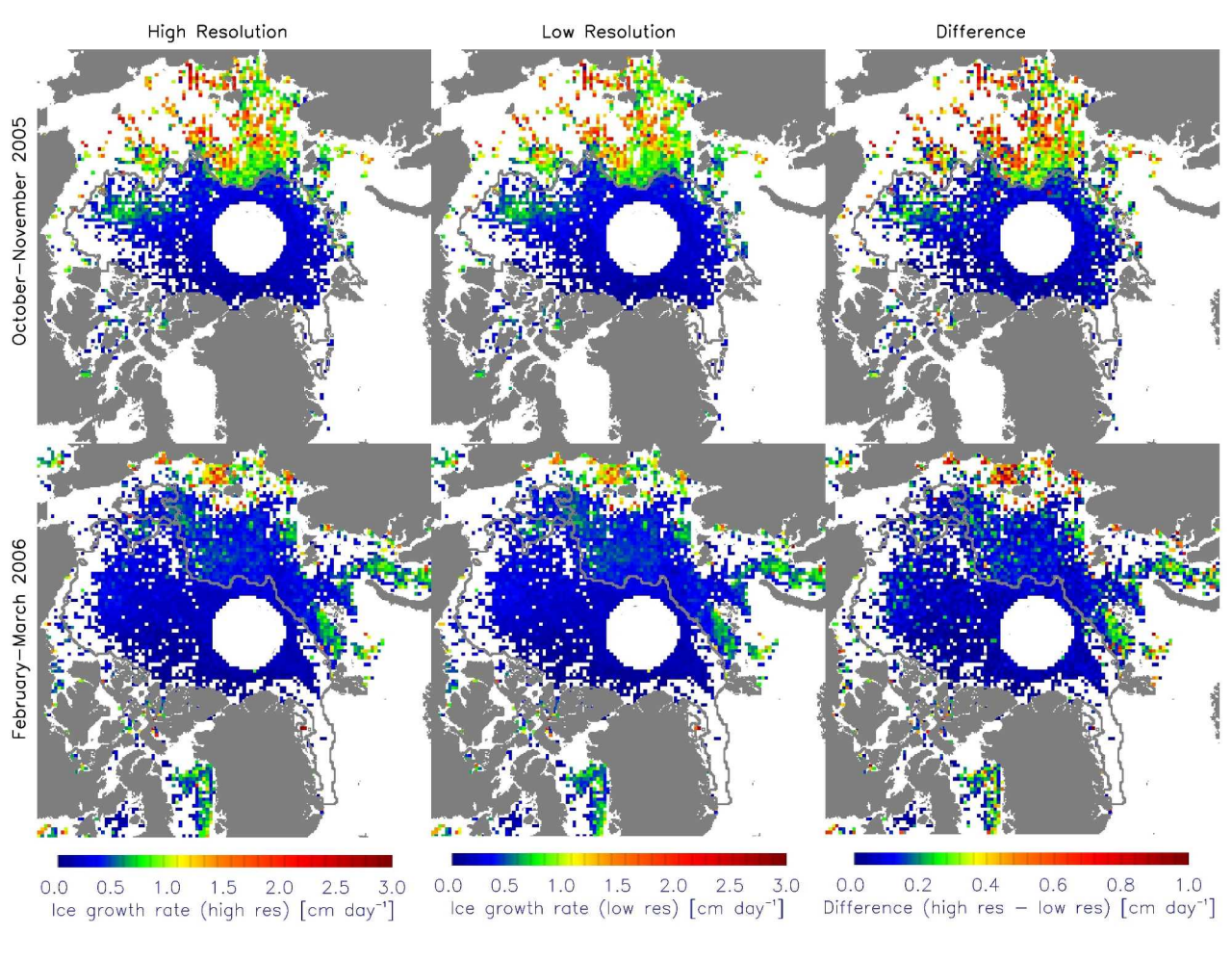
High Resolution
Low Resolution
Difference
October–November 2005
February–March 2006
0.0 0.5 1.0 1.5 2.0 2.5 3.0
Ice growth rate (high res) [cm day⁻¹]
0.0 0.5 1.0 1.5 2.0 2.5 3.0
Ice growth rate (low res) [cm day⁻¹]
0.0 0.2 0.4 0.6 0.8 1.0
Difference (high res – low res) [cm day⁻¹]